

# The Devils in the Point Clouds: Studying the Robustness of Point Cloud Convolutions

Xingyi Li, Wenxuan Wu, Xiaoli Z. Fern, and Li Fuxin

Oregon State University

{lixin, wuwen, xfern, lif}@oregonstate.edu

## Abstract

Recently, there has been a significant interest in performing convolution over irregularly sampled point clouds. Since point clouds are very different from regular raster images, it is imperative to study the generalization of the convolution networks more closely, especially their robustness under variations in scale and rotations of the input data. This paper investigates different variants of PointConv, a convolution network on point clouds, to examine their robustness to input scale and rotation changes. Of the variants we explored, two are novel and generated significant improvements. The first is replacing the multilayer perceptron based weight function with much simpler third degree polynomials, together with a Sobolev norm regularization. Secondly, for 3D datasets, we derive a novel viewpoint-invariant descriptor by utilizing 3D geometric properties as the input to PointConv, in addition to the regular 3D coordinates. We have also explored choices of activation functions, neighborhood, and subsampling methods. Experiments are conducted on the 2D MNIST & CIFAR-10 datasets as well as the 3D SemanticKITTI & ScanNet datasets. Results reveal that on 2D, using third degree polynomials greatly improves PointConv’s robustness to scale changes and rotations, even surpassing traditional 2D CNNs for the MNIST dataset. On 3D datasets, the novel viewpoint-invariant descriptor significantly improves the performance as well as robustness of PointConv. We achieve the state-of-the-art semantic segmentation performance on the SemanticKITTI dataset, as well as comparable performance with the current highest framework on the ScanNet dataset among point-based approaches.

## 1 Introduction

Convolution is one of the most fundamental concepts in deep learning. Convolutional neural networks (CNNs) have redefined the state-of-the-art for almost every task in computer vision. In order to transfer such successes from 2D

images to the 3D world, there is a significant body of work aiming to develop the convolution operation on 3D point clouds. This is essential to many applications such as autonomous driving and virtual/augmented reality.

PointConv [60] seems to be one of the promising efforts. Similar to earlier work [43, 18, 59, 14, 58, 64], PointConv utilizes a multi-layer perceptron (MLP) to learn the convolution weights on each point implicitly as a nonlinear transformation from the point coordinates, basically a Monte Carlo discretization of the continuous convolution operator on irregular point clouds, but with the efficient version of PointConv it now can scale to modern deep networks with dozens of layers. PointConv is permutation-invariant and translation-invariant, and to our best knowledge is the only approach that achieved equivalent performance to 2D CNNs on images as well as having one of the highest performances on 3D benchmarks.

Networks based on point clouds introduce a new complication on the neighborhoods used in convolution. In 2D images, we are accustomed to having fixed-size neighborhoods such as  $3 \times 3$  or  $5 \times 5$ . PointConv and other point-based networks instead adopt k-nearest neighbors (kNN), which may potentially make it harder for point cloud networks to generalize from training locations to testing locations, as sufficiently smooth weight functions need to be learned. Usually, point cloud networks augment the data by randomly jittering point locations, but such jittering only provides local generalization. We attempted to plot one of the typical learnt weight function on MNIST and on a faster-RCNN detector as shown in Fig. 1 (a-b). As one can see, due to the nonlinearity in the weight functions, PointConv could potentially generalize poorly if the testing neighborhoods are substantially different from those of the training. Indeed, even in 2D images we rely on re-scaling of all the images to the same scale to avoid this generalization issue. Such a simple shortcut is, however, unlikely to suffice for point clouds as each kNN neighborhood may be significantly different from others in terms of scale.

In this paper we study empirically the generalization of PointConv under scale changes (resulting in different sam-

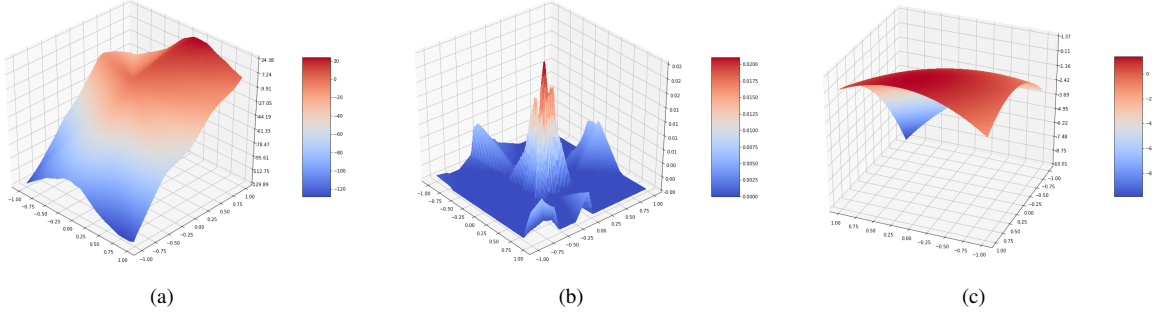


Figure 1: Examples of learned weight functions from PointConv: (a) MLP-based PointConv trained on MNIST; (b) MLP-based PointConv trained with Faster R-CNN; (c) Sobolev-regularized cubic polynomial (Best Viewed in Color)

pling densities) and rotations, which would induce very different neighborhoods between training and testing. The basic methodology is to train the network with a certain set of scales and rotations, and test it on out-of-sample scales/rotations that are significantly different from the training ones. Experiments are done both on the 2D MNIST [25] & CIFAR-10 [22] datasets, and the 3D SemanticKITTI [2] & ScanNet v2 [8] datasets. Multiple design choices are tested, including different neighborhood selection methods, activation functions, input feature transformations and regularization methods to examine their impact on generalization under scale changes and rotations.

From the experiments, we identify two strategies that have not been applied to point cloud networks to be the most effective. In 2D images, we propose to utilize cubic polynomials as the weight functions, with a Sobolev norm regularization similar to thin-plate splines. This restricts the flexibility of the weight functions (Fig. 1) and improves generalization. We additionally find that using an  $\epsilon$ -ball neighborhood is more robust than kNN in 2D. With these improvements, we have found PointConv to be more robust than traditional raster CNNs on scale changes and rotations, which suggests a potential of applying PointConv on 2D images for the sake of robustness in future work.

For 3D point clouds, we introduce a novel viewpoint-invariant (VI) feature transformation to the 3D coordinates. The results show that our novel feature transformation is not only rotation-invariant, but also robust to neighborhood size changes and achieves significantly better generalization results than simply using 3D coordinates as input. VI enables coordinates to generalize to neighborhood of different sizes, hence we have found that  $\epsilon$ -ball neighborhoods become no longer necessary on top of VI. This is welcome news since  $\epsilon$ -ball neighborhoods (e.g. utilized commonly in KPConv [49]) are more expensive to compute than kNN neighborhoods.

## 2 Related Work

**Volumetric and Projection-based Approaches** A direct extension from convolution in 2D raster images to 3D is to compute convolution on volumetric grids [61, 33, 39, 57]. In densely sampled point clouds, sparse volumetric convolutions such as MinkowskiNet [5] and Submanifold sparse convolution [10] currently obtain the best performance. However, they depend heavily on being able to locate enough points in a local volumetric neighborhood of each point, hence are difficult to apply to cases where the sampling density of point clouds is low or especially uneven (e.g. LIDAR). Some other approaches that project point clouds onto multi-view 2D images [46, 36, 30] or lattice space [45] may suffer from the same issue.

**Point-based Approaches** [35] first attempted to directly work on point clouds, and PointNet++ [37] improved it by adding a hierarchical structure. Following PointNet++, some other studies also attempted to utilize hierarchical architectures to aggregate information from neighbor points with MLPs [26, 31]. PointCNN [27] utilized a learned  $X$ -transformation to weight the local features and reorder them simultaneously. FeaStNet [52] utilize a soft-assignment matrix to generalize traditional convolution on point clouds. Flex-convolution [11] introduced a convolution layer for arbitrary metric spaces, along with an efficient GPU implementation. A-CNN [21] proposed an annular convolution that assigned kernel weights for neighbour points based on their distances to the center point. PointWeb [68] considered every pair of points within the neighborhood for extracting contextual features. A-SCN [62] adopt the dot-product self-attention mechanism from [51] to propagate features. PointASNL [65] proposed an adaptive sampling strategy to avoid outliers before extracting local and global features from each point cloud.

Generally, convolutional approaches on point clouds performed better than the approaches listed above. [43, 18, 59, 14, 58, 64] proposed to learn discretizations of continuous convolutional filters. [18] utilized a side network to gener-

ate weights for 2D convolutional kernels. [43] generalized it to 3D point clouds, and [58] further extends it to segmentation tasks [58], along with an efficient version. However, the efficient version in [58] only achieves depthwise convolution rather than full convolution. EdgeConv [59] encodes pairwise features between a neighbor point and the center point through MLPs. [14] takes densities into account. Pointwise CNN [16] located kernel weights for pre-defined voxel bins, so it was not flexible. SpiderCNN [64] proposed a polynomial weight function, which we experiment with in this paper. However, they did not utilize regularization to control the smoothness. The formulation of PointConv [60] is mathematically similar to [14], and it encompasses [43, 59] and [58], since those can be viewed as special cases of PointConv, removing some of the components (e.g. density, full convolution). The main contribution in PointConv [60] is an efficient variant that does not explicitly generate weight functions, but implicitly so by directly computing the convolution results between the weights and the input features. Such a variant removed the memory requirement to store the weights and networks, allowing for scaling up to the “modern” deep network size, e.g. dozens of layers with hundreds of filters per layer. It is also the only paper showing results on CIFAR-10 matching those of a 2D CNN of the same structure.

The main competitive point-based convolutional approach to PointConv is KPConv [49]. In KPConv, convolution weights are generated as kernel functions between each point and anchor points, points in the 3D space that are pre-specified as parameters for each layer separately. KPConv enjoys nice performance due to the smooth and well-regularized kernel formulation, but it introduces significantly more parameters in the specification of anchor points and their  $\epsilon$ -ball neighborhoods are computationally costly. Similar to KPConv, PCNN [1] also assign anchor points with kernel weights, but it does not take neighbor points into account for convolution.

**Scale and rotation invariance in convolution** We did not find significant amount of related work in studying scale and rotation robustness on point clouds. [56, 66] build a spatial transformer side network (STN) to learn global transformations on input point clouds. The main difference comparing with our work is that we aim to improve the robustness against transformations through directly working on the network itself, instead of designing additional structures to accommodate them.

A significant amount of work have been published in 2D CNNs on scale and rotation invariance. A standard approach has been data augmentation [44, 12, 50, 24, 4, 13], where the training set is augmented by including objects with random rescaling or rotations. A group of studies attempted to integrate deep CNNs with side-networks [29, 69, 55, 63, 67, 19] or attention modules [54, 42].

[70] convolved the input with several rotated versions of the same CNN filter before feeding to the pooling layer. Some techniques proposed to learn transformations directly [17, 28] on the input or intermediate outputs from convolutional layers in a deep network [9, 40]. There has also been interest in combining group concepts with CNNs to encode scale and rotate transformations [6, 3, 7].

**Non-deep Approaches** [41] encodes relations between local 3D surface patches as well as global patches in a viewpoint invariant manner, which is a good hint for this work.

### 3 Methodology

The main goal of this work is to investigate how to best enable the learned weight function to generalize from known local locations to unseen ones, to make PointConv [60] based networks more robust against unseen scales and rotations of objects. Toward this, we attempted three methods. First, we replace kNN with  $\epsilon$ -ball based neighbor search to unify the receptive field for each PointConv layer. Next, we introduce a much simpler hypothesis space of third degree polynomials to replace MLP for weight functions to avoid overfitting. To further enforce the smoothness of this hypothesis space, we utilize the Sobolev norm for thin-plate splines as a regularizer. Finally, for 3D point clouds, we introduce a viewpoint-invariant (VI) descriptor for the MLP that utilizes geometric properties of the data to be less sensitive to local scale and rotation changes.

Below we will first introduce PointConv [60], followed by the description of  $\epsilon$ -ball based neighbor search, third degree polynomials, and the VI descriptor for the weight function, respectively.

#### 3.1 Background: PointConv

A point cloud can be denoted as a set of 3D points  $P = \{p_1, p_2, \dots, p_n\}$ , where each point  $p_i$  contains a position vector  $(x, y, z) \in R^3$  as well as a feature vector (RGB color, surface normal, etc.). A line of work including PointConv generalizes the convolution operation to point clouds based on discretizations of continuous 3D convolutions [43, 14, 59, 60]. For a center point  $p_{xyz} = (x, y, z)$ , its PointConv is defined by:

$$PointConv(S, W, F)_{xyz} = \sum_{(\delta_x, \delta_y, \delta_z) \in G} S(\delta_x, \delta_y, \delta_z) W(\delta_x, \delta_y, \delta_z) F(x + \delta_x, y + \delta_y, z + \delta_z) \quad (1)$$

where  $(\delta_x, \delta_y, \delta_z)$  denote the coordinate offsets for a point in  $p_{xyz}$ 's local neighborhood  $G$ , usually located by kNN.  $F(x + \delta_x, y + \delta_y, z + \delta_z)$  represents the feature of the point, and  $W(\delta_x, \delta_y, \delta_z)$  is the convolution kernel generating the weights for convolution and is approximated by an

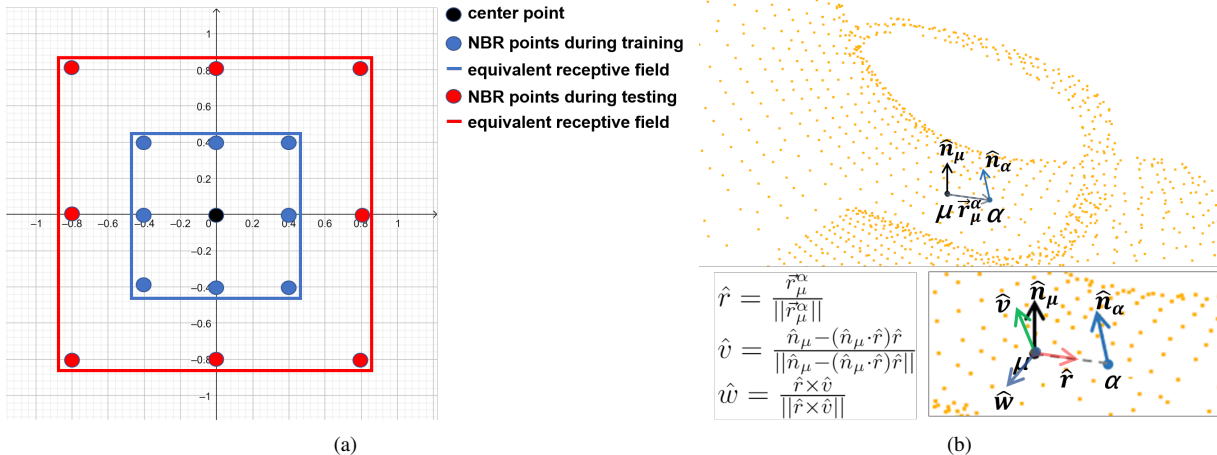


Figure 2: (a) We perform robustness experiments of PointConv on 2D images where the training kNN neighborhood is significantly different from the testing; (b) For a given local center point  $p_\mu$  and  $p_\alpha \in N_\epsilon(p_\mu)$  for a pair of points, a set of viewpoint-agnostic basis  $(\vec{r}, \vec{w}, \vec{v})$  can be generated from  $\vec{r}_\mu^\alpha$  and  $n_\mu$  with the Gram-Schmidt process, and viewpoint-invariant features such as the angles between  $\vec{n}_\mu^\alpha$  and  $\vec{v}$  can be extracted from them

MLP, called *WeightNet* in [60]. Finally,  $S(\delta_x, \delta_y, \delta_z)$  represents the inverse local density to balance the impact of non-uniform sampling of the point clouds.

PointConv uses an efficient approach to avoid the computation of the function values of  $W$  at each point, which is extremely memory-intensive. The computation approach does not change the final output of eq. (1), hence we omit it. A deep network can be built from PointConv layers similar to 2D convolutions. For stride-2 convolution/pooling, one can just subsample the point clouds [37]. [60] also provides a deconvolution/upsampling approach to increase the resolution of point clouds. Hence, classification and semantic segmentation tasks can be solved with PointConv networks. It is also straightforward to incorporate other commonly used 2D convolution operations, e.g. residual connections. Dilated convolution can be approximated by first sampling a larger kNN neighborhood, and then subsampling from the neighborhood.

### 3.2 $\epsilon$ -ball neighbor search and activations

The neighborhood  $G$  in PointConv is usually defined by kNN. Fig. 2 (a) illustrates the robustness issue for K-nearest neighbors search. Namely, the equivalent receptive field for a sparse point cloud is much larger than the one for a densely distributed point cloud. If trained only on dense (high resolution) point clouds, the learned weight function may not generalize well to much larger (unseen) receptive fields when dealing with sparse point clouds during testing.

An  $\epsilon$ -ball based neighborhood (e.g. commonly used in KPConv [49]) on the other hand would be robust to different sampling rates. For a point  $p_i$ , denote  $N_\epsilon(p_i) =$

$\{p_j \in P | d(p_i, p_j) < \epsilon\}$  as its  $\epsilon$ -ball neighborhood. To ease the computation burden, we (randomly) select at most  $K$  neighbors from  $N_\epsilon(p_i)$ . The actual chosen neighbors from  $N_\epsilon(p_i)$  are denoted as  $C_\epsilon(p_i, K)$ . Compared with kNN,  $\epsilon$ -ball neighborhood retains the maximal distance of the neighbors w.r.t. the center point. Since different  $\epsilon$ -balls may contain different number of neighbors, we replace the normalizer  $S(\delta_x, \delta_y, \delta_z)$  in equation 1 with  $\frac{1}{|C_\epsilon(p_i, K)|}$ . Note that the flexibility of the PointConv framework allows for variable number of neighbors in each neighborhood.

We also investigate the robustness over several different activations in the MLP-based WeightNet, such as ReLU [34], SeLU [20], Leaky ReLU [32], and Sine ( $\sin(x)$ ). Sine is included because its connections to random Fourier features [38]. In [38], it was proved that a basis of  $\cos(\mathbf{W}\mathbf{x} + \mathbf{b})$  with random  $\mathbf{W}$  and  $\mathbf{b}$  could be a universal function approximator. Hence we thought learned  $\mathbf{W}$  and  $\mathbf{b}$ s could improve over the pure random one. Empirically we have found that using sine worked better than cosine, maybe due to the fact that  $\sin(0) = 0$  hence it does not introduce additional constants.

### 3.3 Convolutional Kernels as Cubic Polynomials

The set of functions MLPs can represent is very large, which may introduce overfitting to the training point locations. Hence, we experiment with much simpler weight functions  $W(\delta_x, \delta_y, \delta_z)$  in the form of cubic polynomials of  $(x, y, z)$ . This was investigated in [64], however with some arbitrary additional functions multiplied that actually reduced the performance on 2D [60]. We utilize a plain version, with proper weights to regularize for smoothness. In

2D, this results in a feature space:

$$\phi(x, y) = [x^3, y^3, \sqrt{3x^2y}, \sqrt{3xy^2}, \sqrt{3x^2}, \sqrt{3y^2}, \sqrt{6xy}, x, y, 1] \quad (2)$$

and in 3D:

$$\begin{aligned} \phi(x, y, z) = [x^3, y^3, z^3, \sqrt{3x^2y}, \sqrt{3x^2z}, \sqrt{3xy^2}, \sqrt{3y^2z}, \\ \sqrt{3xz^2}, \sqrt{3yz^2}, \sqrt{3x^2}, \sqrt{3y^2}, \sqrt{3z^2}, \sqrt{6xyz}, \sqrt{6xy}, \\ \sqrt{6xz}, \sqrt{6yz}, \sqrt{3x}, \sqrt{3y}, \sqrt{3z}, 1] \end{aligned}$$

The coefficients of each term ensures that an  $L_2$  regularization on the feature descriptors (excluding linear and constant terms) correspond to regularizing with the Sobolev  $S_2$  norm:

$$\|f\|_{s_2}^2 = \lambda \int \int [(\frac{\partial^2 f}{\partial x^2})^2 + 2(\frac{\partial^2 f}{\partial x \partial y})^2 + (\frac{\partial^2 f}{\partial y^2})^2] dx dy \quad (3)$$

in 2D, where  $\lambda$  is a parameter. The 3D form can be written similarly. Sobolev-norm regularizations are commonly used in thin-plate splines [53] but to our knowledge they have not been used in point cloud networks in the past. Note that the choice of a third degree polynomial is common in the smoothing splines community. Quadratic functions have undesirable symmetries and fourth-order polynomials introduce too many terms, e.g. 35 terms for a 3D space.

### 3.4 A Viewpoint-Invariant Input Descriptor

PointConv relies on the  $(x, y, z)$  coordinates to compute the weights, which is sensitive to the rotation of the object as well as the sampling rate of the point clouds. We hypothesize that by using viewpoint-invariant descriptors for the weight function, we can achieve better generalization.

We develop a viewpoint-invariant (VI) descriptor for each point  $p_\alpha$  in a local neighborhood as an 8-dimensional vector utilizing its geometric relationship with the center point  $p_\mu$ . Denote the surface normal of  $p_\mu$  as  $\hat{n}_\mu$  and its difference with  $p_\alpha$  as  $\vec{r}_\mu^\alpha = p_\alpha - p_\mu$ . When the scene is rotated, the angle between  $\hat{n}_\mu$  and  $\vec{r}_\mu^\alpha$  remains the same. To discriminate between different directions, we generate an orthonormal basis from  $\{\hat{n}_\mu, \vec{r}_\mu^\alpha\}$  and compute the angles between  $\hat{n}_\mu, \vec{r}_\mu^\alpha$  and  $\hat{n}_\alpha$  as well as the projection lengths of  $\hat{n}_\alpha$  and  $\hat{n}_\mu$  onto the orthonormal basis. With a global rotation of the scene, the basis and normal vectors are identically rotated. Hence, our descriptor is rotation invariant and provides a complete characterization of the vectors  $\hat{n}_\mu, \vec{r}_\mu^\alpha$  and  $\hat{n}_\alpha$ .

Formally, we utilize the Gram-Schmidt process on  $\{\vec{r}_\mu^\alpha, \hat{n}_\mu\}$  to generate a 3D basis  $\{\hat{r}, \hat{v}, \hat{w}\}$  where  $\hat{r} = \frac{\vec{r}_\mu^\alpha}{\|\vec{r}_\mu^\alpha\|}$ ,  $\hat{v} = \frac{\hat{n}_\mu - (\hat{r}^\top \hat{n}_\mu) \hat{r}}{\sqrt{1 - (\hat{r}^\top \hat{n}_\mu)^2}}$  is orthonormal to  $\hat{r}$ , and  $\hat{w}$  is derived by  $\hat{r} \times \hat{v}$ , the outer product of  $\hat{r}$  and  $\hat{v}$ , as illustrated in Fig. 2. Note that this basis is seldom degenerate, because it is unlikely for  $\hat{n}_\mu$  and  $\vec{r}_\mu^\alpha$  to be collinear in 3D surface point clouds.

With the basis defined, for each point  $p_\alpha$  in the neighborhood of  $p_\mu$ , we extract the following viewpoint invariant feature vector:

$$\beta_\mu^\alpha = [\hat{n}_\alpha \cdot \hat{n}_\mu, \frac{\vec{r}_\mu^\alpha \cdot \hat{n}_\mu}{\|\vec{r}_\mu^\alpha\|}, \frac{\vec{r}_\mu^\alpha \cdot \hat{n}_\alpha}{\|\vec{r}_\mu^\alpha\|}, \hat{n}_\alpha \cdot \hat{v}, \hat{n}_\alpha \cdot \hat{w}, \frac{\vec{r}_\mu^\alpha \cdot \hat{n}_\mu, \vec{r}_\mu^\alpha \cdot (\hat{n}_\alpha \times \hat{n}_\mu), \|\vec{r}_\mu^\alpha\|}{\|\vec{r}_\mu^\alpha\|}] \quad (4)$$

where  $\times$  represents the cross product. The first 5 features are both scale and rotation invariant, and the last 3 features are rotation invariant only. We believe that a weight function with this input will be invariant to rotation and more robust against scale changes. We also anticipate this to alleviate the need for rotation-based data augmentation.

## 4 Experiments

### 4.1 MNIST

MNIST contains 60,000 handwritten digits in the training set and 10,000 digits in the test set from 10 distinct classes. The original resolution of each image is  $28 \times 28$ . We trained a 4-layer network. Table 1 illustrate the general architecture for our proposed framework and all other baselines. They only differ in the structures for convolutional layers. The  $\epsilon$  is fixed to  $\frac{1}{10}$  for Conv1 in Table 1,  $\frac{1}{5}$  for Conv2, and  $\frac{1}{2}$  for Conv3 as well as Conv4. The numbers of output points from FPS for Subsampling1 Subsampling2 layer in Table 1 are 196 and 49 respectively. The coefficient of the Sobolev norm regularization is set to  $10^{-6}$  or  $10^{-5}$  for our proposed approach. For other ablation variants, it was tuned to the optimal one. We utilize cross entropy as the loss function. The batch size is 60 and the optimizer is Adam with learning rate 0.001. For traditional 2D CNN baselines, we adopt max pooling with  $2 \times 2$  stride for the sub-sampling layer. Global average pooling is used in the last layer to account for different input resolutions. For point cloud sub-sampling, we attempt two different methods. The first one is named as PC-2D subsampling, which achieves the equivalent number of sampled points as 2D max-pooling with stride  $2 \times 2$ , but in point cloud formats. The next one is Farthest Point Sampling (FPS), a commonly used sampling approach in point cloud networks [37, 60].

To convert a 2D raster image with the resolution of  $m \times n$  to a point cloud, we generate a point for each pixel with normalized coordinates  $p_i(x, y) = (\frac{m_i}{m}, \frac{n_i}{n}) \in R^2$  as its spatial location. Normalization constrains the input range of each coordinate for the weight function to  $[0, 1]$ . Thus, images of different scales are converted to point clouds with different sampling densities. The original RGB feature is also normalized to  $[0, 1]$ .

Three 2D CNN baselines are considered. The first one is exactly the same structure as the PointConv network. The other two utilize the Deformable CNN [9], and

Layer name	Layer description
Conv1	$3 \times 3$ conv. (or PointConv) 64 w/ ReLU
Subsampling1	max-pooling with stride $2 \times 2$ (or farthest point sampling)
Conv2	$3 \times 3$ conv. (or PointConv) 128 w/ ReLU
Subsampling2	max-pooling with stride $2 \times 2$ (or farthest point sampling)
Conv3	$3 \times 3$ conv. (or PointConv) 128 w/ ReLU
Conv4	$3 \times 3$ conv. (or PointConv) 128 w/ ReLU
Pooling	global average pooling
FC-10	fully connected layer
Softmax layer	

Table 1: The general network architecture for MNIST experiments. Every convolutional layer is followed by a ReLU layer.

CapsNet [40] respectively. Both claimed to be robust to scale/rotation changes. Every baseline is tuned to the optimal performance based on the validation accuracy.

**Robustness to Scaling** The first experiment we conduct is to train with images of limited known scales and test on larger/smaller objects outside of the known scales. To construct the training set, all MNIST images are rescaled to  $20 \times 20$ ,  $28 \times 28$ , and  $36 \times 36$ , respectively. The validation set is built by rescaling the original test images to  $24 \times 24$  and  $32 \times 32$ . We trained all baseline models on this new MNIST dataset, and tuned parameters on the validation set. Test accuracies are measured on images with  $34 \times 34$ ,  $38 \times 38$ ,  $44 \times 44$ ,  $56 \times 56$ ,  $72 \times 72$ ,  $18 \times 18$ ,  $14 \times 14$ , and  $10 \times 10$  resolutions, which creates a discrepancy with training.

Results are shown in Table 2 and 3. PC-2D sampling is generally inferior to the furthest point subsampling. We note several takeaways:

- Naive kNN-based PointConv is less robust to scale changes than conventional CNN. On most out-of-sample scales it does not generalize as well as the 2D CNNs.
- Cubic polynomials with Sobolev regularization outperforms MLP with any activation at most scales. Sobolev regularization improves robustness especially at small scales.
- $\epsilon$ -ball neighborhood is generally more robust than kNN neighborhood, especially at scales significantly different from the training.
- With appropriate design e.g. cubic polynomial WeightNet and  $\epsilon$ -ball neighborhood, PointConv is significantly more robust to scale changes than traditional 2D CNN.

This builds a case to use PointConv in 2D spaces with an  $\epsilon$ -ball neighborhood, and a cubic polynomial WeightNet with Sobolev regularizations. Especially, the significantly

improved robustness w.r.t. 2D CNNs may justify the use of PointConv even for 2D raster images, if robustness is of concern.

**Robustness to Rotations** The next experiment we conduct is to train with objects of limited known rotations and test on objects with various rotated angles. We define counter clockwise as the positive rotation direction. The training set is constructed through rotating the original  $28 \times 28$  training images (or point clouds) by  $-15^\circ$ ,  $0^\circ$ , and  $+15^\circ$  around the center. We rotate the original testing images (or point clouds) by  $-15^\circ$  and  $+15^\circ$  to create the validation set. All parameters are tuned on the validation dataset. Test accuracies are measured on the rotation angles of  $\pm 10^\circ$ ,  $\pm 20^\circ$ , and  $\pm 40^\circ$ .

Trends on results shown in Table 4 are similar to those mentioned in the previous subsection, e.g.  $\epsilon$ -ball and cubic polynomials outperform kNN and MLPs. However, here the regular ReLU seems to show the most robustness among the activation functions, although cubic polynomials still outperform all the MLP-based WeightNets. With  $\epsilon$ -ball and cubic polynomials, PointConv is again significantly more robust than regular CNNs. Interestingly CapsNet is able to show better rotation robustness than PointConv. Given that CapsNet is orthogonal to PointConv, it maybe possible to combine them in future work.

## 4.2 CIFAR-10

In CIFAR-10 [22], there are 60,000 RGB images in 10 classes in the training set, and 10,000 images in the test set. The original size of each image is  $32 \times 32$ . The general architecture of all baselines are shown in Table 5. We adopt the same hyperparameters and preprocessing procedures as detailed in section 4.1, besides the Sobolev norm regularizer. The  $\epsilon$  is fixed to 0.05 for Conv1 in Table 5, 0.1 for Conv2 and Conv3, 0.2 for Conv4 and Conv5, and 0.5 for Conv6 as well as Conv7. The numbers of output points from FPS for Subsampling1, Subsampling2, and Subsampling3 layer in Table 5 are 256, 64, and 16, respectively.

# NBR	Neighborhood	WeightNet architecture	34 × 34	38 × 38	44 × 44	56 × 56	72 × 72	18 × 18	14 × 14	10 × 10
16	$\epsilon$ -ball	cubic P + Sobolev Reg.	95.37%	94.35%	<b>94.56%</b>	<b>94.01%</b>	<b>93.23%</b>	<b>95.82%</b>	<b>96.15%</b>	47.4%
9	$\epsilon$ -ball	cubic P + Sobolev Reg.	91.96%	93.31%	91.00%	92.20%	91.04%	95.51%	95.27%	<b>68.83%</b>
9	kNN	cubic P + Sobolev Reg.	93.78%	93.84%	90.21%	88.45%	69.41%	92.79%	84.56%	54.67%
9	kNN	cubic P	90.31%	94.35%	89.77%	90.42%	68.46%	91.37%	81.73%	24.02%
9	kNN	MLP w/ Sine	91.35%	92.91%	84.69%	79.45%	66.29%	86.06%	74.61%	31.6%
9	kNN	MLP w/ SeLU	91.77%	90.52%	87.5%	82.66%	69.5%	91.74%	82.9%	38.18%
9	kNN	MLP w/ Leaky ReLU	95.57%	88.89%	80.69%	49.8%	37.89%	94.61%	81.22%	26.85%
9	kNN	MLP w/ ReLU	71.38%	75.04%	75.41%	51.33%	18.85%	69.23%	59.54%	29.88%
CNN			96.30%	95.68%	89.19%	51.23%	25.77%	75.6%	24.25%	11.2%
Deformable CNN			91.31%	16.05%	17.99%	11.56%	11.35%	74.40%	28.18%	14.74%
CapsNet			<b>98.53%</b>	<b>97.52%</b>	93.28%	43.25%	16.50%	80.07%	21.41%	8.65%

Table 2: MNIST performance comparison across different scales under the setting of farthest subsampling. P is short for polynomials, and NBR is short for neighbor. The first row indicates the resolution of test images.

# NBR	Neighborhood	WeightNet architecture	34 × 34	38 × 38	44 × 44	56 × 56	72 × 72	18 × 18	14 × 14	10 × 10
16	$\epsilon$ -ball	cubic P + Sobolev Reg.	95.83%	96.21%	<b>97.84%</b>	<b>97.92%</b>	<b>98.23%</b>	90.8%	64.47%	21.78%
9	$\epsilon$ -ball	cubic P + Sobolev Reg.	94.76%	95.58%	96.56%	96.89%	97.27%	<b>93.51%</b>	<b>88.20%</b>	<b>23.59%</b>
9	kNN	cubic P + Sobolev Reg.	97.64%	96.83%	95.92%	54.06%	23.99%	53.84%	17.98%	10.11%
9	kNN	cubic P	97.85%	97.31%	95.38%	42.71%	13.77%	14.77%	12.02%	7.28%
9	kNN	MLP w/ Sine	95.76%	94.35%	94.47%	47.26%	19.02%	76.5%	30.01%	10.86%
9	kNN	MLP w/ SeLU	92.03%	82.49%	56.90%	17.09%	6.01%	33.78%	10.51%	11.59%
9	kNN	MLP w/ Leaky ReLU	66.27%	24.39%	13.69%	10.11%	10.1%	65.66%	16.50%	8.11%
9	kNN	MLP w/ ReLU	16.54%	16.66%	11.35%	11.35%	11.35%	10.63%	7.83%	6.43%
CNN			96.30%	95.68%	89.19%	51.23%	25.77%	75.6%	24.25%	11.2%
Deformable CNN			91.31%	16.05%	17.99%	11.56%	11.35%	74.40%	28.18%	14.74%
CapsNet			<b>98.53%</b>	<b>97.52%</b>	93.28%	43.25%	16.50%	80.07%	21.41%	8.65%

Table 3: MNIST performance comparison across different scales under the setting of PC-2D subsampling. P is short for polynomials, and NBR is short for neighbor. The first row indicates the resolution of test images.

# NBR	Neighborhood	WeightNet architecture	+10°	-10°	+20°	-20°	+40°	-40°
12	$\epsilon$ -ball	cubic P + Sobolev Reg.	96.93%	96.63%	96.2%	95.86%	85.27%	<b>85.51%</b>
9	$\epsilon$ -ball	cubic P + Sobolev Reg.	95.52%	95.58%	94.63%	94.55%	81.27%	84.27%
9	kNN	cubic P + Sobolev Reg.	98.11%	97.68%	95.96%	97.2%	64.79%	63.71%
9	kNN	cubic P	98.50%	98.37%	95.52%	97.45%	56.23%	61.75%
9	kNN	MLP w/ Sine	98.11%	97.65%	93.84%	93.95%	20.21%	29.27%
9	kNN	MLP w/ SeLU	97.75%	97.56%	43.27%	94.66%	10.44%	11.62%
9	kNN	MLP w/ Leaky ReLU	98.09%	97.56%	92.34%	95.71%	36.16%	35.49%
9	kNN	MLP w/ ReLU	98.03%	97.62%	92.65%	95.53%	37.03%	34.39%
CNN			96.47%	96.9%	95.06%	95.51%	75.71%	74.28%
Deformable CNN			98.21%	98.60%	96.59%	97.60%	80.82%	81.01%
CapsNet			<b>99.8%</b>	<b>99.9%</b>	<b>99.6%</b>	<b>99.5%</b>	<b>92.5%</b>	83.8%

Table 4: MNIST performance comparison with different rotations under the setting of farthest subsampling. P stands for polynomials, and NBR stands for neighbor. The first row indicates the rotation angles of test images.

The coefficient of the Sobolev norm regularization is set to one of  $\{10^{-6}, 10^{-5}, 10^{-4}\}$  for our proposed approach. We does not adopt PC-2D subsampling since it is experimen-

tally proven not robust in 4.1.

Two 2D CNN baselines are considered. The first one is the traditional CNN as shown in Table 5, and the other

Layer name	Layer description
Conv1	$3 \times 3$ conv. (or PointConv) 64 w/ BN & ReLU
Subsampling1	max-pooling with stride $2 \times 2$ (or farthest point sampling)
Conv2	$3 \times 3$ conv. (or PointConv) 128 w/ BN & ReLU
Conv3	$3 \times 3$ conv. (or PointConv) 128 w/ BN & ReLU
Subsampling2	max-pooling with stride $2 \times 2$ (or farthest point sampling)
Conv4	$3 \times 3$ conv. (or PointConv) 256 w/ BN & ReLU
Conv5	$3 \times 3$ conv. (or PointConv) 256 w/ BN & ReLU
Subsampling3	max-pooling with stride $2 \times 2$ (or farthest point sampling)
Conv6	$3 \times 3$ conv. (or PointConv) 512 w/ BN & ReLU
Conv7	$3 \times 3$ conv. (or PointConv) 512 w/ BN & ReLU
Pooling	global average pooling
FC-10	fully connected layer
Softmax layer	

Table 5: The general network architecture for CIFAR-10 experiments. BN stands for batch normalization. Every BN layer is followed by a ReLU layer.

one is Deformable CNN [9] which has the exact architecture except for that the last four convolutional layer are deformable. We did not including CapsNet [40] in this experiment, since it has no pooling layers and performs poorly on this dataset.

**Robustness to Scaling** The first experiment tests robustness with respect to scaling. The original training set is augmented to three different resolutions, which are  $24 \times 24$ ,  $32 \times 32$ , and  $40 \times 40$ , respectively. The validation resolutions are  $28 \times 28$ , and  $36 \times 36$ . We trained all baseline models on this new CIFAR-10 dataset, and tuned hyperparameters on the validation set.

Results are shown in Table 6. We note several take-aways:

- Naive kNN-based PointConv is less robust to scale changes than conventional CNN. On most out-of-sample scales it does not generalize as well as the 2D CNNs. Even for the resolution  $32 \times 32$ , the generalization is less well than traditional CNNs. This is interesting since we have verified that with the same architecture PointConv is able to match CNN performance if trained only under a single resolution, which might show that further work is needed for PointConv to be robust to mixing resolutions in training.
- Cubic polynomials outperform MLP with any activation at most scales. Sobolev regularization does not universally improve the robustness against scaling on this dataset.
- $\epsilon$ -ball neighborhood is generally significantly more robust than kNN neighborhood when testing scales are significantly different from the training.
- With appropriate design e.g. cubic polynomial WeightNet and an  $\epsilon$ -ball neighborhood, PointConv

is significantly more robust than traditional 2D CNN when the testings scales that are significantly larger/smaller than training scales.

**Robustness to Rotations** The next experiment we conduct is to train baselines with images with a few predefined rotations, and test them on images with various rotated angles. The counter clockwise direction is defined as the positive direction. To construct the training set, we rotate the original  $32 \times 32$  training images (or point clouds) by  $-15^\circ$ ,  $0^\circ$ , and  $+15^\circ$  around the center. The validation set is created through rotating the original testing images (or point clouds) by  $-15^\circ$  and  $+15^\circ$ . All parameters are tuned on the validation dataset. Test accuracies are measured on the rotation angles of  $\pm 10^\circ$ ,  $\pm 20^\circ$ , and  $\pm 40^\circ$ .

The corresponding results are shown in Table 7. We observe that  $\epsilon$ -ball still outperforms kNN in all nonzero rotations but underperform it at no rotation. However, Leaky ReLU is overall comparable with cubic polynomial with Sobolev regularization as the best approach, and SeLU performed significantly worse. Besides, PointConv is generally significantly less robust as regular or deformable CNNs in this case, showing that more work needs to be done in terms of robustness to rotations in 2D in more complex datasets.

### 4.3 ScanNet

We conduct 3D semantic scene segmentation on the ScanNet v2 [8] dataset. We use the official split with 1, 201 scenes for training and 312 for validation.

We implemented 2 PointConv architectures. One is the 4-layer network in [60], the second one is the 16-layer PointConv network that achieved 66.6% on the ScanNet testing set. Network architectures are provided by the authors. Our main results are reported on the ScanNet valida-



# NBR	Neighborhood	WeightNet architecture	$32 \times 32$	$48 \times 48$	$60 \times 60$	$76 \times 76$	$88 \times 88$	$22 \times 22$	$18 \times 18$	$16 \times 16$
16	$\epsilon$ -ball	cubic P + Sobolev Reg.	73.43%	70.24%	<b>68.56%</b>	<b>65.7%</b>	<b>65.78%</b>	66.15%	<b>67.12%</b>	<b>71.89%</b>
9	$\epsilon$ -ball	cubic P + Sobolev Reg.	70.56%	68.00%	67.15%	64.41%	65.31%	59.89%	63.36%	66.41%
9	kNN	cubic P + Sobolev Reg.	78.59%	61.67%	46.32%	32.48%	24.91%	64.67%	52.50%	59.65%
9	kNN	cubic P	78.09%	61.87%	47.12%	30.91%	27.63%	63.17%	54.48%	59.65%
9	kNN	MLP w/ Sine	71.29%	39.62%	30.58%	26.69%	25.17%	46.68%	21.99%	23.81%
9	kNN	MLP w/ SeLU	72.04%	47.27%	37.48%	34.81%	34.54%	35.21%	18.51%	23.80%
9	kNN	MLP w/ Leaky ReLU	76.06%	16.85%	9.85%	11.37%	11.21%	41.56%	30.11%	27.47%
9	kNN	MLP w/ ReLU	69.58%	20.81%	15.00%	12.01%	12.36%	38.89%	27.17%	25.32%
CNN			<b>88.47%</b>	<b>79.21%</b>	59.21%	38.43%	27.13%	<b>69.11%</b>	44.99%	39.80%
Deformable CNN			82.82%	72.03%	52.07%	31.91%	25.68%	60.20%	51.20%	45.67%

Table 6: CIFAR-10 performance comparison across different scales under the setting of farthest subsampling. P is short for polynomials, and NBR is short for neighbor. The first row indicates the resolution of test images.

# NBR	Neighborhood	WeightNet architecture	$0^\circ$	$+10^\circ$	$-10^\circ$	$+20^\circ$	$-20^\circ$	$+40^\circ$	$-40^\circ$
12	$\epsilon$ -ball	cubic P + Sobolev Reg.	71.26%	67.63%	67.55%	64.58%	65.36%	40.13%	42.64%
9	$\epsilon$ -ball	cubic P + Sobolev Reg.	69.72%	66.24%	66.56%	63.13%	63.71%	39.42%	39.42%
9	kNN	cubic P + Sobolev Reg.	75.57%	62.95%	60.12%	59.96%	54.35%	42.94%	39.13%
9	kNN	cubic P	75.94%	62.27%	59.12%	57.18%	54.68%	38.85%	37.61%
9	kNN	MLP w/ Sine	68.32%	45.11%	44.11%	35.92%	35.52%	15.35%	16.34%
9	kNN	MLP w/ SeLU	69.04%	43.81%	41.26%	40.83%	37.97%	21.53%	18.28%
9	kNN	MLP w/ Leaky ReLU	78.01%	65.68%	64.84%	59.22%	57.85%	34.67%	34.14%
9	kNN	MLP w/ ReLU	76.79%	64.57%	62.25%	57.43%	55.21%	31.07%	33.98%
CNN			<b>86.61%</b>	83.72%	<b>84.48%</b>	<b>78.03%</b>	78.25%	45.71%	46.14%
Deformable CNN			86.53%	<b>83.74%</b>	83.96%	77.69%	<b>78.31%</b>	<b>47.21%</b>	<b>47.72%</b>

Table 7: CIFAR-10 performance comparison with different rotations under the setting of farthest subsampling. P stands for polynomials, and NBR stands for neighbor. The first row indicates the rotation angles of test images.

tion set as the benchmark organizers do not allow ablation studies on the testing set.

We adopt regular subsampling [48] for feature encoding layers with grid sizes 0.05, 0.1, 0.2, and 0.4 (in meter).  $\epsilon$  is set to be  $\frac{1}{1.3}$  of the grid size for the corresponding subsampling layer. We enumerated  $\epsilon$  in  $\{\frac{1}{1.0}, \frac{1}{1.1}, \frac{1}{1.2}, \frac{1}{1.3}, \frac{1}{1.4}, \frac{1}{1.5}\}$ , and it turned out the network is not sensitive to those choices (see supplementary for experiments). The surface normal for a subsampled point is computed through averaging all surface normals of its corresponding grid. During training, we randomly subsample 100,000 points from each point cloud for both the training and validation sets, and the mini-batch size is set to be 3. The learning rate is set to  $10^{-3}$ , with a decay multiplier of  $\frac{1}{2}$  every 40 epochs. Moreover, the rotation augmentation is applied by randomly rotating every mini-batch with an arbitrary angle in  $[0, 2\pi)$ , as in [60].

To study the robustness to scales for all baselines, we re-sample each validation point cloud to less than  $100k$  —  $\{60k, 40k, 20, 10k\}$ . This is equivalent to downsampling the image in the 2D space as it increases the size of KNN

neighborhoods with a fixed  $K$ . Also, each sub-sampled point cloud is further rotated with 4 different predefined angles around  $z$ -axis —  $\{0^\circ, 90^\circ, 180^\circ, 270^\circ\}$ . Such operations could significantly change both local scales and rotations. We also evaluate the performance when the rotation augmentation is not applied during training. We found performance variation between different rotation angles to be less than 1% (see supplementary), hence the mIoUs averaged from all angles are reported. Experiments are performed with the proposed VI descriptor, as well as configurations that are promising from 2D experiments:  $\epsilon$ -ball, cubic polynomial WeightNet, and SeLU activation.

Results are shown in Table 8, which shows that the proposed VI descriptor significantly improved the performance as well as robustness under every setting. Especially, it is significantly more robust to input downsampling than the  $(x, y, z)$  coordinates as input. For example, at  $10k$  testing points (reflecting  $10x$  downsampling from the training), the VI descriptors still maintain a 44.7% accuracy while the  $(x, y, z)$  coordinates version has its performance dropped to 17.8%, marking an improvement of 251%. Besides, with VI

# layers	MLP input	activation	NBR setting	rotation augmentation	100k	60k	40k	20k	10k
16	VI + $(x, y, z)$	ReLU	KNN	Y	<b>68.2</b>	<b>64.4</b>	<b>63.0</b>	<b>57.6</b>	45.4
16	VI	ReLU	KNN	Y	63.3	60.7	59.7	55.0	44.7
16	VI	SeLU	KNN	Y	63.7	61.5	57.7	53.1	40.2
16	VI	Cubic First Block + ReLU in others	KNN	Y	63.5	61.4	60.2	54.0	42.0
16	$(x, y, z)$	ReLU	KNN	Y	61.7	58.7	53.4	34.6	17.8
16	VI	ReLU	KNN	N	60.4	58.6	57.8	54.2	46.3
16	$(x, y, z)$	ReLU	KNN	N	56.4	54.0	51.2	40.6	27.4
16	VI	ReLU	$\epsilon$ -ball	Y	61.61	58.6	58.0	52.3	40.6
16	$(x, y, z)$	ReLU	$\epsilon$ -ball	Y	48.9	43.3	39.7	30.6	20.7
16	surface normal + $(x, y, z)$	ReLU	KNN	Y	60.2	57.5	56.8	54.8	50.9
16	surface normal	ReLU	KNN	Y	53.1	50.6	50.2	47.6	43.3
4	VI + $(x, y, z)$	ReLU	KNN	Y	64.5	61.3	60.6	57.3	<b>51.2</b>
4	VI	ReLU	KNN	Y	61.0	58.8	57.5	50.8	39.4
4	$(x, y, z)$	ReLU	KNN	Y	55.3	53.3	47.0	30.7	16.1
4	VI	ReLU	$\epsilon$ -ball	Y	59.2	57.5	55.12	44.8	31.1

Table 8: Performance results (mIoU,%) for the ScanNet dataset. The first column shows the configurations of the approach, and the top row contains the number of subsampled points. The default number of neighbors is 8, and the default activation for weight functions is ReLU.

descriptor, the need to use rotation augmentation reduced significantly. Interestingly, rotation augmentation still improved performance by 2%. We believe the main reason is that the input feature of our framework consists of both  $(x, y, z)$  coordinates and RGB colors, and thus rotation augmentation creates more  $(x, y, z)$  coordinates variations for the training, and hence improved performance. We further conduct ablation studies by replacing VI descriptors with surface normals. The mIoU drops by 8% – 10%, which indicates that VI is a better representation of local geometry than the commonly used surface normal.

Finally, when we combined the VI features with  $(x, y, z)$  inputs, it generated the best performance of all – 68.2% on the original validation set, and better on almost all subsampled scenarios. This shows that a combination of scale-invariant, rotation-invariant and non-invariant features is beneficial, potentially letting the network choose the invariance it requires. Furthermore, on the test set, we achieved comparable mIoU with KPConv [49], which is the current state-of-the-art among point-based approaches (Table 9). Note that PointConv [60] has significantly less parameters than KPConv [49], and KNN used in PointConv is significantly more efficient than the  $\epsilon$ -ball in KPConv.

Otherwise, none of the other tested choices were helpful, including  $\epsilon$ -ball, SeLU or cubic polynomial. Our takeaway is that the proposed VI descriptor is very powerful and improved robustness significantly w.r.t. neighborhood sizes, hence, none of the other improvements is needed.

From our experience, it is very difficult to find a good set

of parameters for  $\epsilon$ -ball in 3D. It also slows down the algorithm because the non-uniform neighborhood size is not easily amenable for tensor computation. Hence not needing to use it is a significant bonus. Nevertheless,  $\epsilon$ -ball neighborhoods are still very useful in 2D settings, where locating them is much easier and the VI descriptor is not applicable.

Method	mIoU(%)
PointNet++ [37]	33.9
SPLATNet [45]	39.3
TangentConv [47]	40.9
PointCNN [27]	45.8
PointASNL [65]	63.0
PointConv [60]	66.6
KPConv [49]	<b>68.4</b>
VI-PointConv (ours)	67.6

Table 9: Semantic Scene Segmentation results for point-based approaches on the ScanNet test set

#### 4.4 SemanticKITTI

We also evaluate the semantic segmentation performance on SemanticKITTI [2] (single scan), which consists of 43, 552 point clouds sampled from 22 sequences in driving scenes. Each point cloud contains 10–13k points, collected by a single Velodyne HDL-64E laser scanner, spanning up to  $160 \times 160 \times 20$  meters in 3D space. The officially training

Method	mIoUs(%)	road	sidewalk	parking	other-ground	building	car	truck	bicycle	motorcycle	other-vehicle	vegetation	trunk	terrain	person	bicyclist	motorcyclist	fence	pole	traffic-sign
PointNet[35]	14.6	61.6	35.7	15.8	1.4	41.4	46.3	0.1	1.3	0.3	0.8	31.0	4.6	17.6	0.2	0.2	0.0	12.9	2.4	3.7
SPG[23]	17.4	45.0	28.5	0.6	0.6	64.3	49.3	0.1	0.2	0.2	0.8	48.9	27.2	24.6	0.3	2.7	0.1	20.8	15.9	0.8
SPLATNet[45]	18.4	64.6	39.1	0.4	0.0	58.3	58.2	0.0	0.0	0.0	0.0	71.1	9.9	19.3	0.0	0.0	0.0	23.1	5.6	0.0
PointNet++[37]	20.1	72.0	41.8	18.7	5.6	62.3	53.7	0.9	1.9	0.2	0.2	46.5	13.8	30.0	0.9	1.0	0.0	16.9	6.0	8.9
TangentConv[47]	40.9	83.9	63.9	33.4	15.4	83.4	90.8	15.2	2.7	16.5	12.1	79.5	49.3	58.1	23.0	28.4	8.1	49.0	35.8	28.5
PointConv[60]	53.0	86.2	68.6	57.7	16.0	89.9	94.2	30.2	29.5	33.9	30.5	78.9	60.8	63.7	48.8	45.7	20.4	59.9	53.4	38.6
RandLA-Net[15]	53.9	<b>90.7</b>	<b>73.7</b>	60.3	20.4	86.9	94.2	40.1	26.0	25.8	38.9	81.4	61.3	66.8	49.2	48.2	7.2	56.3	49.2	47.7
KPConv[49]	58.8	88.8	72.7	61.3	31.6	90.5	<b>96.0</b>	33.4	30.2	<b>42.5</b>	44.3	<b>84.8</b>	<b>69.2</b>	<b>69.1</b>	<b>61.5</b>	<b>61.6</b>	11.8	64.2	56.5	47.4
VI-PCConv(ours)	<b>59.6</b>	88.8	72.5	<b>63.5</b>	<b>32.7</b>	<b>91.4</b>	95.9	<b>41.8</b>	<b>38.6</b>	35.0	<b>45.7</b>	83.9	68.0	66.9	51.2	50.1	<b>27.6</b>	<b>66.6</b>	<b>57.4</b>	<b>54.8</b>

Table 10: Semantic Scene Segmentation results for point-based approaches on the SemanticKITTI test set

set includes 19,130 scans (sequences 00 – 07 and 09 – 10), and there are 4,071 scans (sequence 08) for validation. For each 3D point, only  $(x, y, z)$  coordinate is given without any color information. It is a challenging dataset because faraway points are sparser in LIDAR scans.

We adopt the exact same 16-layer architecture as showed at the first row of Table 8, together with the mini-batch size of 16. The initial learning rate is  $10^{-3}$ , and it is decayed by half every 6 epochs. We do not integrate with any subsampling preprocessing. As reported in Table 10, we achieve the state-of-the-art semantic segmentation performance among point-based baselines, improving by 0.8% over KPConv and 6.6% over standard PointConv, which demonstrate the effectiveness of VI descriptor for PointConv [60].

## 5 Conclusion

This paper empirically studies several strategies to improve the robustness for point cloud convolution with PointConv [60]. We have found two combinations to be effective. In 2D images, using an  $\epsilon$ -ball neighborhood with cubic polynomial weight functions achieved the highest robustness, and outperformed 2D CNNs for MNIST dataset. In 3D images, our novel viewpoint-invariant descriptor, when used instead of, or in combination with the 3D coordinates, significantly improved the performance and robustness of PointConv networks and achieved state-of-the-art. Our results show that kNN is still a viable neighborhood choice if the input location features are robust to neighborhood sizes.

## References

[1] Matan Atzmon, Haggai Maron, and Yaron Lipman. Point convolutional neural networks by extension operators. *international conference on computer graphics and interactive techniques*, 2018.

[2] J. Behley, M. Garbade, A. Milioto, J. Quenzel, S. Behnke, C. Stachniss, and J. Gall. SemanticKITTI: A Dataset for Semantic Scene Understanding of LiDAR Sequences. In *Proc. of the IEEE/CVF International Conf. on Computer Vision (ICCV)*, 2019.

[3] Arunkumar Byravan and Dieter Fox. Se3-nets: Learning rigid body motion using deep neural networks. In *International Conference on Robot and Automation*, 2017.

[4] Gong Cheng, Peicheng Zhou, and Junwei Han. Rifd-cnn: Rotation-invariant and fisher discriminative convolutional neural networks for object detection. In *The IEEE Conference on Computer Vision and Pattern Recognition (CVPR)*, June 2016.

[5] Christopher Choy, JunYoung Gwak, and Silvio Savarese. 4d spatio-temporal convnets: Minkowski convolutional neural networks. In *Proceedings of the IEEE Conference on Computer Vision and Pattern Recognition*, pages 3075–3084, 2019.

[6] Taco Cohen and Max Welling. Group equivariant convolutional networks. In *International Conference on Machine Learning*, pages 2990–2999, 2016.

[7] Taco S Cohen and Max Welling. Steerable cnns. In *ICLR*, 2017.

[8] Angela Dai, Angel X. Chang, Manolis Savva, Maciej Halber, Thomas Funkhouser, and Matthias Nießner. Scannet: Richly-annotated 3d reconstructions of indoor scenes. In *Proc. Computer Vision and Pattern Recognition (CVPR), IEEE*, 2017.

[9] Jifeng Dai, Haozhi Qi, Yuwen Xiong, Yi Li, Guodong Zhang, Han Hu, and Yichen Wei. Deformable convolutional networks. In *ICCV*, 2017.

[10] Benjamin Graham, Martin Engelcke, and Laurens van der Maaten. 3d semantic segmentation with submanifold sparse convolutional networks. *CVPR*, 2018.

[11] Fabian Groh, Patrick Wieschollek, and Hendrik P. A. Lensch. Flex-convolution (million-scale point-cloud learning beyond grid-worlds). In *Asian Conference on Computer Vision (ACCV)*, Dezember 2018.

- [12] Kaiming He, Xiangyu Zhang, Shaoqing Ren, and Jian Sun. Spatial pyramid pooling in deep convolutional networks for visual recognition. In *ECCV*. 2014.
- [13] João F. Henriques and Andrea Vedaldi. Warped convolutions: Efficient invariance to spatial transformations. In *Proceedings of the International Conference on Machine Learning (ICML)*, 2017.
- [14] P. Hermosilla, T. Ritschel, P-P Vazquez, A. Vinacua, and T. Ropinski. Monte carlo convolution for learning on non-uniformly sampled point clouds. *ACM Transactions on Graphics (Proceedings of SIGGRAPH Asia 2018)*, 37(6), 2018.
- [15] Qingyong Hu, Bo Yang, Linhai Xie, Stefano Rosa, Yulan Guo, Zhihua Wang, Niki Trigoni, and Andrew Markham. Randla-net: Efficient semantic segmentation of large-scale point clouds. *Proceedings of the IEEE Conference on Computer Vision and Pattern Recognition*, 2020.
- [16] Binh-Son Hua, Minh-Khoi Tran, and Sai-Kit Yeung. Point-wise convolutional neural networks. In *Computer Vision and Pattern Recognition (CVPR)*, 2018.
- [17] Max Jaderberg, Karen Simonyan, Andrew Zisserman, et al. Spatial transformer networks. In *NIPS*, pages 2017–2025, 2015.
- [18] Xu Jia, Bert De Brabandere, Tinne Tuytelaars, and Luc V Gool. Dynamic filter networks. In D. D. Lee, M. Sugiyama, U. V. Luxburg, I. Guyon, and R. Garnett, editors, *Advances in Neural Information Processing Systems 29*, pages 667–675. Curran Associates, Inc., 2016.
- [19] Yonghyun Kim, Bong-Nam Kang, and Daijin Kim. San: Learning relationship between convolutional features for multi-scale object detection. In *ECCV*, 2018.
- [20] Günter Klambauer, Thomas Unterthiner, Andreas Mayr, and Sepp Hochreiter. Self-normalizing neural networks. In I. Guyon, U. V. Luxburg, S. Bengio, H. Wallach, R. Fergus, S. Vishwanathan, and R. Garnett, editors, *Advances in Neural Information Processing Systems 30*, pages 971–980. Curran Associates, Inc., 2017.
- [21] Artem Komarichev, Zichun Zhong, and Jing Hua. A-cnn: Annularly convolutional neural networks on point clouds. In *Proceedings of the IEEE Conference on Computer Vision and Pattern Recognition*, 2019.
- [22] A. Krizhevsky. Learning multiple layers of features from tiny images. In *Tech Report*, 2009.
- [23] L. Landrieu and M. Simonovsky. Large-scale point cloud semantic segmentation with superpoint graphs. In *2018 IEEE/CVF Conference on Computer Vision and Pattern Recognition*, pages 4558–4567, 2018.
- [24] Dmitry Laptev, Nikolay Savinov, Joachim M Buhmann, and Marc Pollefeys. Ti-pooling: transformation-invariant pooling for feature learning in convolutional neural networks. In *Proceedings of the IEEE Conference on Computer Vision and Pattern Recognition*, pages 289–297, 2016.
- [25] Yann LeCun, Corinna Cortes, and Christopher J.C. Burges. The mnist database of handwritten digits. 1998.
- [26] Jiaxin Li, Ben M. Chen, and Gim Hee Lee. So-net: Self-organizing network for point cloud analysis. In *The IEEE Conference on Computer Vision and Pattern Recognition (CVPR)*, 2018.
- [27] Yangyan Li, Rui Bu, Mingchao Sun, Wei Wu, Xinhan Di, and Baoquan Chen. Pointcnn: Convolution on x-transformed points. In S. Bengio, H. Wallach, H. Larochelle, K. Grauman, N. Cesa-Bianchi, and R. Garnett, editors, *Advances in Neural Information Processing Systems 31*, pages 820–830. Curran Associates, Inc., 2018.
- [28] Chen-Hsuan Lin and Simon Lucey. Inverse compositional spatial transformer networks. In *IEEE Conf. Comput. Vis. Pattern Recog.*, 2017.
- [29] Tsung-Yi Lin, Piotr Dollar, Ross Girshick, Kaiming He, Bharath Hariharan, and Serge Belongie. Feature pyramid networks for object detection. In *CVPR*, 2017.
- [30] Yiqun Lin, Zizheng Yan, Haibin Huang, Dong Du, Ligang Liu, Shuguang Cui, and Xiaoguang Han. Fpconv: Learning local flattening for point convolution. In *IEEE/CVF Conference on Computer Vision and Pattern Recognition (CVPR)*, June 2020.
- [31] Xinhai Liu, Zhizhong Han, Yu-Shen Liu, and Matthias Zwicker. Point2sequence: Learning the shape representation of 3d point clouds with an attention-based sequence to sequence network. In *Thirty-Third AAAI Conference on Artificial Intelligence*, 2019.
- [32] Andrew L. Maas, Awni Y. Hannun, and Andrew Y. Ng. Rectifier nonlinearities improve neural network acoustic models. In *in ICML Workshop on Deep Learning for Audio, Speech and Language Processing*, 2013.
- [33] Daniel Maturana and Sebastian Scherer. Voxnet: A 3d convolutional neural network for real-time object recognition. In *2015 IEEE/RSJ International Conference on Intelligent Robots and Systems (IROS)*, pages 922–928. IEEE, 2015.
- [34] Vinod Nair and Geoffrey E. Hinton. Rectified linear units improve restricted boltzmann machines. In Johannes Fürnkranz and Thorsten Joachims, editors, *ICML*, pages 807–814. Omnipress, 2010.
- [35] Charles R Qi, Hao Su, Kaichun Mo, and Leonidas J Guibas. Pointnet: Deep learning on point sets for 3d classification and segmentation. *arXiv preprint arXiv:1612.00593*, 2016.
- [36] Charles Ruizhongtai Qi, Hao Su, Matthias Nießner, Angela Dai, Mengyuan Yan, and Leonidas Guibas. Volumetric and multi-view cnns for object classification on 3d data. In *Proc. Computer Vision and Pattern Recognition (CVPR)*, IEEE, 2016.
- [37] Charles R Qi, Li Yi, Hao Su, and Leonidas J Guibas. Pointnet++: Deep hierarchical feature learning on point sets in a metric space. *arXiv preprint arXiv:1706.02413*, 2017.
- [38] Ali Rahimi and Benjamin Recht. Random features for large-scale kernel machines. In *Advances in neural information processing systems*, pages 1177–1184, 2008.
- [39] Gernot Riegler, Ali Osman Ulusoy, and Andreas Geiger. Octnet: Learning deep 3d representations at high resolutions. In *Proceedings of the IEEE Conference on Computer Vision and Pattern Recognition*, 2017.
- [40] Sara Sabour, Nicholas Frosst, and Geoffrey E Hinton. Dynamic routing between capsules. In *NIPS*. 2017.
- [41] Rahul Sawhney, Fuxin Li, Henrik I. Christensen, and Charles L. Isbell Jr. Purely geometric scene association and retrieval - A case for macro scale 3d geometry. *CoRR*, abs/1808.01343, 2018.

- [42] Shikhar Sharma, Ryan Kiros, and Ruslan Salakhutdinov. Action recognition using visual attention. In *NIPS Time Series Workshop*. 2015.
- [43] M. Simonovsky and N. Komodakis. Dynamic edge-conditioned filters in convolutional neural networks on graphs. In *2017 IEEE Conference on Computer Vision and Pattern Recognition (CVPR)*, pages 29–38, 2017.
- [44] Karen Simonyan and Andrew Zisserman. Very deep convolutional networks for large-scale image recognition. In *ICLR*, 2015.
- [45] Hang Su, Varun Jampani, Deqing Sun, Subhransu Maji, Evangelos Kalogerakis, Ming-Hsuan Yang, and Jan Kautz. SPLATNet: Sparse lattice networks for point cloud processing. In *Proceedings of the IEEE Conference on Computer Vision and Pattern Recognition*, pages 2530–2539, 2018.
- [46] Hang Su, Subhransu Maji, Evangelos Kalogerakis, and Erik G. Learned-Miller. Multi-view convolutional neural networks for 3d shape recognition. In *Proc. ICCV*, 2015.
- [47] Maxim Tatarchenko\*, Jaesik Park\*, Vladlen Koltun, and Qian-Yi Zhou. Tangent convolutions for dense prediction in 3D. *CVPR*, 2018.
- [48] H. Thomas, F. Goulette, J. Deschaud, B. Marcotegui, and Y. LeGall. Semantic classification of 3d point clouds with multiscale spherical neighborhoods. In *2018 International Conference on 3D Vision (3DV)*, pages 390–398, 2018.
- [49] Hugues Thomas, Charles R. Qi, Jean-Emmanuel Deschaud, Beatriz Marcotegui, François Goulette, and Leonidas J. Guibas. Kpconv: Flexible and deformable convolution for point clouds. *Proceedings of the IEEE International Conference on Computer Vision*, 2019.
- [50] David A van Dyk and Xiao-Li Meng. The art of data augmentation. *Journal of Computational and Graphical Statistics*, 10(1):1–50, 2001.
- [51] Ashish Vaswani, Noam Shazeer, Niki Parmar, Jakob Uszkoreit, Llion Jones, Aidan N Gomez, Łukasz Kaiser, and Illia Polosukhin. Attention is all you need. In I. Guyon, U. V. Luxburg, S. Bengio, H. Wallach, R. Fergus, S. Vishwanathan, and R. Garnett, editors, *Advances in Neural Information Processing Systems 30*, pages 5998–6008. Curran Associates, Inc., 2017.
- [52] Nitika Verma, Edmond Boyer, and Jakob Verbeek. FeaStNet: Feature-Steered Graph Convolutions for 3D Shape Analysis. In *CVPR - IEEE Conference on Computer Vision & Pattern Recognition*, pages 2598–2606, Salt Lake City, United States, June 2018. IEEE.
- [53] G. Wahba. *Spline Models for Observational Data*. Society for Industrial and Applied Mathematics, Philadelphia, 1990.
- [54] Fei Wang, Mengqing Jiang, Chen Qian, Shuo Yang, Cheng Li, Honggang Zhang, Xiaogang Wang, and Xiaoou Tang. Residual attention network for image classification. In *CVPR*, 2017.
- [55] Hao Wang, Qilong Wang, Mingqi Gao, Peihua Li, and Wangmeng Zuo. Multi-scale location-aware kernel representation for object detection. In *CVPR*, 2018.
- [56] Jiayun Wang, Rudrasis Chakraborty, and Stella X. Yu. Spatial transformer for 3d points. *CoRR*, abs/1906.10887, 2019.
- [57] Peng-Shuai Wang, Yang Liu, Yu-Xiao Guo, Chun-Yu Sun, and Xin Tong. O-CNN: Octree-based Convolutional Neural Networks for 3D Shape Analysis. *ACM Transactions on Graphics (SIGGRAPH)*, 36(4), 2017.
- [58] Shenlong Wang, Simon Suo, Wei-Chiu Ma, Andrei Pokrovsky, and Raquel Urtasun. Deep parametric continuous convolutional neural networks. In *The IEEE Conference on Computer Vision and Pattern Recognition (CVPR)*, June 2018.
- [59] Yue Wang, Yongbin Sun, Ziwei Liu, Sanjay E. Sarma, Michael M. Bronstein, and Justin M. Solomon. Dynamic graph cnn for learning on point clouds. *ACM Transactions on Graphics (TOG)*, 2019.
- [60] Wenxuan Wu, Zhongang Qi, and Li Fuxin. Pointconv: Deep convolutional networks on 3d point clouds. In *The IEEE Conference on Computer Vision and Pattern Recognition (CVPR)*, June 2019.
- [61] Zhirong Wu, Shuran Song, Aditya Khosla, Fisher Yu, Linguang Zhang, Xiaoou Tang, and Jianxiong Xiao. 3d shapenets: A deep representation for volumetric shapes. In *Proceedings of the IEEE conference on computer vision and pattern recognition*, pages 1912–1920, 2015.
- [62] Saining Xie, Sainan Liu, Zeyu Chen, and Zhuowen Tu. Attentional shapecontextnet for point cloud recognition. In *Proceedings of the IEEE Conference on Computer Vision and Pattern Recognition (CVPR)*, June 2018.
- [63] Hongyu Xu, Xutao Lv, Xiaoyu Wang, Zhou Ren, Navaneeth Bodla, and Rama Chellappa. Deep regionlets for object detection. In *ECCV*, 2018.
- [64] Yifan Xu, Tianqi Fan, Mingye Xu, Long Zeng, and Yu Qiao. Spidercnn: Deep learning on point sets with parameterized convolutional filters. In *The European Conference on Computer Vision (ECCV)*, September 2018.
- [65] Xu Yan, Chaoda Zheng, Zhen Li, Sheng Wang, and Shuguang Cui. Pointasnl: Robust point clouds processing using nonlocal neural networks with adaptive sampling. In *IEEE/CVF Conference on Computer Vision and Pattern Recognition (CVPR)*, June 2020.
- [66] Wentao Yuan, David Held, Christoph Mertz, and Martial Hebert. Iterative transformer network for 3d point cloud. *arXiv preprint arXiv:1811.11209*, 2018.
- [67] Rui Zhang, Sheng Tang, Yongdong Zhang, Jintao Li, and Shuicheng Yan. Scale-adaptive convolutions for scene parsing. *ICCV*, 2017.
- [68] Hengshuang Zhao, Li Jiang, Chi-Wing Fu, and Jiaya Jia. PointWeb: Enhancing local neighborhood features for point cloud processing. In *CVPR*, 2019.
- [69] Peng Zhou, Bingbing Ni, Cong Geng, Jianguo Hu, and Yi Xu. Scale-transferrable object detection. In *CVPR*, June 2018.
- [70] Yanzhao Zhou, Qixiang Ye, Qiang Qiu, and Jianbin Jiao. Oriented response networks. In *CVPR*, 2017.